Blade Load Unsteadiness and Turbulence Statistics in an Actuator-Line Computed Turbine-Turbine Interaction Problem

Pankaj K. Jha
Graduate Research Assistant
Department of Aerospace Engineering, The Pennsylvania State University
229 Hammond Building
University Park, PA 16802
pkj107@psu.edu

Sven Schmitz[1]
Assistant Professor
Department of Aerospace Engineering, The Pennsylvania State University
229 Hammond Building
University Park, PA 16802
sus52@engr.psu.edu

ABSTRACT

The objective of this study is to investigate how different volumetric projection techniques used in actuator-line modeling affect the unsteady blade loads and wake turbulence statistics. The two techniques for the body-force projection radius are based on either i) the grid spacing, or ii) the combination of grid spacing and an equivalent elliptic blade planform. An array of two National Renewable Energy Laboratory 5-MW turbines separated by seven rotor diameters is simulated for 2,000 sec (about rotor 300 revolutions) within a large-eddy simulation solver of the neutral and moderately-convective atmospheric boundary layer. The statistics of sectional angle of attack, blade loads, and turbine power histories are quantified. Moreover, the degree of unsteadiness of sectional blade loads in response to atmospheric and wake turbulence is computed via a reduced frequency based on the rate of change in sectional angle of attack. The goal of this work is to make the wind energy community aware of the uncertainties associated with actuator-line modeling approaches.

[1] Corresponding Author.

I. INTRODUCTION

The wind industry faces a number of challenges today in developing wind farms both onshore and offshore. One such challenge involves wind turbine wakes that interact with turbines located downstream, with other wakes, and with the turbulent atmospheric boundary layer (ABL). The ABL has different stability states during a diurnal cycle, which strongly affect the structure and strength of the ABL's turbulence, thus affecting the array efficiency in a wind farm **[**1**]**. At this time, fully blade-resolved simulations subject to resolved turbulent inflow are only possible with hybrid Reynolds-averaged Navier-Stokes (RANS)/Large-Eddy Simulation (LES) **[**3**]**. These high-fidelity simulations represent the current state-of-the-art in high-performance computing of wind turbine blades; however, the associated computational cost is too exorbitant for routine use, hence precluding the simulation of an entire wind plant using this approach. The actuator-line method (ALM), on the other hand, offers the potential for accurately predicting unsteady wind turbine wakes at an affordable computational cost. The ALM was originally developed by Sørensen and Shen **[**5**]**, and further work was done by their coworkers enhancing the model and applying it to operating wind farms subject to different inflow conditions and for different types of rotors **[**6**]**. The ALM has recently been implemented into an ABL-LES solver created with the OpenFOAM computational fluid dynamics toolbox **[**10**]** by researchers at the National Renewable Energy Laboratory (NREL). The solver has demonstrated its potential to model large wind farms and overall wake effects [11-17].

Apart from the popular ALM, other actuator-type methods that are commonly in use are the actuator disk method (ADM) and actuator surface method (ASM). Some simpler models, for example **[**18**]**, also exist where the focus is to study the geometry of the tip vortices for an optimal turbine. A notable work using such a turbine model was published by Okulov and Sørensen **[**19**]**. The focus of this work was the maximum efficiency of a rotor with constant circulation distribution along the blade (Joukowsky rotor). The method is based on an analytical solution to the problem of equilibrium motion of a helical vortex in a far wake. The ADM, despite being of lower fidelity compared to ALM, is a robust method when the problem of concern is the overall wind farm performance and flow patterns in the farm. This type of study has been performed by several researchers who studied different aspects of a fully-developed wind farm operation, for example the optimal spacing of the turbines, asymptotic behavior of wakes, and staggered and aligned configurations for different turbines [20-23]. A further detailed study has been presented recently in the work by VerHulst and Meneveau **[**24**]**. They have shown how kinetic energy is entrained into large wind turbine arrays and, in particular, how large-scale flow structures contribute to such entrainment. Several other researchers have performed dedicated investigations of specific aspects of the flow pattern in a wind farm. While Nathan et. al. **[**25**]** dedicated their study to the near wake, Okulov and Sørensen **[**26**]** concentrated on the far wake. Their focus was the stability of tip vortices in the far wake. On the other hand, Viola et. al. **[**27**]** performed a dedicated study on the stability of hub/root vortices. These studies indeed complement one

another. A very recent unprecedented study by Hong et. al. [28] revealed the large-scale flow structures in the wake of a 2.5 MW wind turbine using natural snowfall.

Most of the works discussed above were concerned with the power output and wake propagation. The authors believe that a complementary work focusing on blade-loads statistics and unsteadiness will add to the growing understanding of wind farm dynamics. A great attempt in this direction has been made by Chatelain et. al. [29] who used a vortex-particle mesh method with immersed lifting lines, relying on the Lagrangian discretization of the Navier–Stokes equations in vorticity-velocity formulation while studying blade loads and turbulence statistics with an emphasis on wake meandering. The turbulent inflow was either obtained from a precursor ABL or purely synthetic. The type of inflow is important for a computational study of wind farm dynamics, since it defines the large-scale ABL structures. Synthetic turbulent inflow, however, lacks the ability to predict coherent structures [30]. A need for a better understanding of the unsteady blade-load response of the turbines and the challenges involved in modeling the former was addressed by Leishman [31].

In summary, very little work has been done in the wind energy scientific community where the influence of the ALM modeling approaches with respect to the unsteady blade loads and wake turbulence statistics are addressed. Recent work by the authors addressed some difficulties of the ALM in accurately predicting sectional blade loads, in particular at the blade tips, suggesting some modifications to the ALM [32-34].

The contribution of this work lies in answering the important question of how variations in the ALM modeling approach affect the statistics and unsteady

aerodynamics response of blade loads in conjunction with time trace and statistics of integrated power for a turbine-turbine interaction problem of two NREL 5-MW turbines separated by seven rotor diameters and submerged in ABL flow of neutral and moderately-convective stability states. It is found that i) ALM modeling parameters lead to a notable uncertainty in power predictions attributed to differences in blade loads at the outer 15% of blade span and ii) unsteady aerodynamics occurs predominantly at inboard blade stations and are less pronounced at the outboard part of the blade where differences in ALM approaches are dominant.

II. NUMERICAL METHODS

The numerical method underlying the problem consists of two parts. The first one is the simulation of atmospheric boundary-layer flow, and the second one is the simulation of an array of two turbines using the ALM. The following subsections describe these two parts.

A. Atmospheric Boundary-Layer Simulation

The atmospheric boundary layer is simulated within a Large-Eddy Simulation (LES) framework using the OpenFOAM CFD toolbox **[**10**]**. The ABL simulation, which includes atmospheric stability effects, serves as a precursor to the wind farm simulation. The governing equations and detailed information on the different terms in the continuity, momentum, and potential temperature equations are explained in earlier works [11-12]. The ABL simulation takes surface roughness height, surface temperature flux, mean wind speed and direction etc. as inputs. Periodic boundary conditions are

applied on the sides. The simulation is run until a quasi-stationary state is achieved, which is different for the two ABL states considered in this work and is typically 6-7 large-eddy turnover times. Following this, the flow data at the inlet plane(s) are saved for the time duration for which the wind farm simulation is intended. The approach in this work is similar to that used by Steven et al. **[**30**]** to generate physical ABL coherent structures.

B. Actuator-Line Method (ALM) and Wake Simulation

The ALM is rooted in the work of Sørensen and Shen **[**5**]** and is being actively developed, maintained and enhanced by the researchers at NREL **[**10**]**, The Pennsylvania State University [32-34], and others. The ALM-ABL solver is a 2nd order, unstructured finite-volume solver. The ALM finds sectional lift and drag forces by determining the local flow velocity and angle of attack (AOA) that is then applied to an airfoil lift/drag lookup table. The blade is discretized into a finite number (typically 25-40) of actuator elements. The lift and drag forces computed at the center of these actuator elements are then projected onto the background Cartesian grid as the volumetric body forces in the momentum equation of the flow solver. These body forces are the reaction of the fluid to the rotor blade forces. The last term in the momentum equation (1) corresponds to this body force,

$$\frac{Du}{Dt} = RHS + F_P \qquad (1)$$

The body-force term indirectly imposes a pressure jump across the actuator line. The projection of the element-wise blade loads into a volumetric body force is typically achieved by a Gaussian projection function as shown in equation (2),

$$F_P(x_P, y_P, z_P) = -\sum_N \sum_m f_{N,m}(x_{N,m}, y_{N,m}, z_{N,m})\,\eta_{N,m} \tag{2}$$

where $$\eta_{N,m} = \exp\left[-\left(\frac{|r|}{\varepsilon}\right)^2\right] / \left(\varepsilon^3 \pi^{3/2}\right) \quad . \tag{3}$$

Here *N* is the blade index, *m* is the actuator point index, and $|\boldsymbol{r}|$ is the distance from the grid cell to the actuator point. Recent advances were made by the authors [32-34] on varying the body-force projection width, or Gaussian radius ε, such that an improved prediction of the spanwise blade loads was obtained without the need for a tip-loss correction. This was accomplished by using a variable Gaussian radius, ε, along the blade span that is determined using an equivalent elliptic planform, c*. Details can be found in a recent paper [33]. In this work, the following techniques for determining ε are used for quantitative comparisons:

Grid-based ε $\quad \varepsilon / \Delta r = const. = 2$

Elliptic ε $\quad \varepsilon / c^* = f(r, \Delta r, AR)$ **[33]** (4)

The first of these, the grid-based method, is the standard method that is widely used, and the second method is a result of recent improvements **[**32**]**. As mentioned above, the focus of this work is to answer the questions of how these two techniques for determining the body-force projection width, or Gaussian radius ε, affect the time-

varying blade loads and integrated power, the associated turbulence statistics in the wake, and the degree of blade loads unsteadiness.

The ALM simulations, forced by precursor boundary-layer data (see section II.A), are performed on grids of type and resolution that the authors have found to give accurate and consistent results **[**32**]**. An illustration is given in Fig. 1. Typically, 3 to 4 layers of grid refinement are performed in the region surrounding the turbines and their wakes, starting with the original grid used for the ABL precursor simulation. A grid resolution of 2.5 m near the turbine is used as a baseline. This is the finest grid resolution of the innermost grid, and it is maintained up to the end of the region of interest to allow for the proper resolution of the smaller-scale turbulent structures generated by the turbine blades and the turbine wakes. The resulting total number of grid cells is close to 25 million.

III. RESULTS AND DISCUSSION

A. Atmospheric Boundary-Layer Simulation

The ABL simulations were performed for a neutral boundary layer (NBL) and a moderately-convective boundary layer (MCBL) with a surface-temperature flux of 0.04 K-m/s. The surface roughness was chosen to be 0.001 m, which is typical for the ABL over sea [11]. The wind speed at hub height (90 m) was forced to be 8 m/s for the precursor simulation. This was achieved by altering the pressure gradient in the governing momentum equation. The grid used had the dimensions: 3 km x 3 km x 1 km with a coarse resolution of 10 m, which is coarser than the actual grid used for ALM

simulations. This is done to ensure that the ABL simulation reaches a quasi-stationary state with available computational resources. The quasi-stationary state, determined by the convergence of the horizontally-averaged friction velocity, was found to be achieved at 18,000 s for NBL and 10,000 s for MCBL. The quasi-stationary state is reached earlier for MCBL than for NBL because of enhanced mixing due to buoyancy-driven turbulence. Integrated boundary-layer properties, turbulent structures, energy spectra, and velocity profiles in the ABL have been presented by the authors in a recent paper [35]. In the case of MCBL, strong updrafts due to the temperature flux at the surface were identified that do not occur in the NBL. Both NBL and MCBL precursor data were used as ABL inflow to a turbine-turbine interaction problem consisting of two NREL 5-MW turbines [36] separated by 7 rotor diameters (D), see Fig. 1(b). The results are presented and discussed in the following sections.

B. An Array of Two NREL 5-MW Turbines in NBL and MCBL Flow at V_{Hub} = 8 m/s

The simulations with the two turbines were performed for 2,000 s for which stored precursor ABL inflow data were available. The averaging was done starting at 300 sec when the initial transients had disappeared. The near-blade grid resolution was 2.5 m, and the time step of the ALM simulation was smaller compared to the precursor ABL simulations such that the actuator-line tips do not traverse more than one grid cell per time step. This constraint is similar to a CFL criterion based on the rotor tip speed. The time-step size was chosen to be 0.02 s corresponding to an average azimuthal step of 1.1 degree. Stored precursor ABL inflow data were used as inflow boundary conditions; the opposite boundaries were outflow boundaries. As the precursor boundary-data time

interval need not coincide with the ALM simulation time step, the boundary data are linearly interpolated in time.

The selected time interval of 1,700 seconds, corresponding to 260 revolutions, is adequate to yield meaningful turbulence statistics, since the wake is fully evolved. The horizontally-averaged mean velocity at hub height from the ABL simulation was 8 m/s, for NBL as well as MCBL, see Fig. 1(b). This was achieved by altering the pressure gradient in the ABL solver, and this velocity at hub height served as a reference velocity. The actual ALM simulation did not have this constraint. The velocity profiles were sampled along a vertical line passing through a line connecting the turbine hubs, for the entire 2,000 s of simulation time, saving line data every 1 sec (or 50 time steps).

Figure 2 shows instantaneous flow fields at t = 2,000 sec. Iso-contours of the z-component of vorticity are shown for the two types of body-force projection methods discussed earlier and for NBL inflow. It can be seen that the wakes for the two cases exhibit indiscernible differences. However, it is unclear from Fig. 2 what the quantitative differences of the two ALM approaches are. In the following, sectional AOA, which is the most fundamental physical parameter relevant to the ALM, and blade loads, are discussed. In particular, the statistics, probability density function (PDF), and power spectral density (PSD) are quantified. Next, the integrated quantities, in particular power, are analyzed. The blade loads affect the tip vortices and vortex sheets emanating from the turbines. Therefore, the effect of the ALM projection method on wake turbulence, and hence the inflow to the downstream turbine, are quantitatively assessed.

B1. Distribution of Angle of Attack (AOA) along Turbine Blades

The underlying method of any ALM starts with the determination of the flow-field velocity vector at the actuator points. These velocity components determine the local AOA at a given actuator point at each time step. Figure 3 shows spanwise distributions of sectional mean and standard deviation (indicated as error bars) of AOA along the blades of both turbines, for both ABL stability states, and for both ALM projection methods. Results are shown for one blade at a time contrasting the two ALM spreading methods considered in this work. It can be observed in all the cases that a constant Gaussian spreading radius $\varepsilon/\Delta_{grid}$ leads to higher AOA at the blade tips compared to those computed with the elliptic Gaussian radius ε/c^*. It should be noted that no tip correction was applied to the airfoil data and that these are instantaneous AOA responses; the effect of adding a simple dynamic stall model is addressed in section III.B.4. Both types of ALM spreading methods yield similar AOA distributions inboard of r/R = 0.85. In general, the inboard stations show higher mean as well as standard deviation. This can be attributed to the fact that the angular velocity component is smaller inboard compared to outboard sections along the blades. Therefore, it has less contribution to the local relative velocity. Hence the inboard local velocity vector is more sensitive to changes in the axial-inflow wind speed than its outboard counterpart. It can be seen that the local mean AOAs for turbine 1 in Fig. 3(a) and 3(c) are not that different for the two ABL stability states. In general, the mean AOAs are smaller for turbine 2 than for turbine 1 for both ABL conditions. This is, as will be shown later, because of the wake velocity deficit experienced by the second turbine. It should be

noted that the rotor speed is torque controlled. Consequently, the rotor speed of turbine 1 remains close to the design speed. Turbine 2 tries to track the design tip speed ratio (TSR) in response to the velocity deficit in the wake but, because of rotor inertia, it cannot do this instantaneously. The difference in AOA for turbine 2 in Fig. 3(b) and 3(d) is more pronounced for NBL than for MCBL because vertical turbulent mixing in the MCBL accelerates the recovery process of the wake velocity deficit. We can therefore conclude that the mean wind (or axial) component of the resultant velocity compared to the local angular velocity component is higher in the MCBL than in the NBL, thus resulting in turbine 2 having a higher mean AOA in MCBL flow than in NBL flow. The standard deviations in AOAs are, in general, larger for turbine 2 than for turbine 1 and for both ABL states because turbine 2 encounters turbulence due to both the ABL as well as the wake of turbine 1. Also, the turbine wakes meander, so the blades of turbine 2 operate in both waked and unwaked flow.

The statistics presented above take into account the entire simulation time interval after the wake of the upstream turbine 1 starts interacting with the downstream turbine 2, i.e. t = 300 sec – 2,000 sec. One question that arises, though, is how likely the local AOA is to lie within a certain range as this has implications on attached and separated flow regions along the blade span. This can be studied by looking at the probability density function (PDF) of the local AOA at selected radial stations of relevance. Figure 4 shows the PDFs of the AOA for the two turbines and at the spanwise locations r/R = 0.340 and r/R = 0.914 that represent one inboard and one outboard blade station. Comparisons are performed for the two types of ALM spreading

for the Gaussian radius ε and the two ABL states. For both turbines and both ABL stability states, constant $\varepsilon/\Delta_{grid}$ spreading moves the PDF curve to a higher mean AOA at the outboard location r/R=0.914, which reflects the higher AOA observed in Fig. 3. The ALM spreading method does not shift the curves at the inboard location r/R = 0.340. Smaller AOAs for turbine 2 are again observed, consistent with Fig. 3. Both inboard and outboard, the ABL state does not cause a shift in the curve for turbine 1. However, this is different for turbine 2 where the PDFs are shifted to higher mean AOA for MCBL inflow, i.e. the AOAs for turbine 2 are higher in a MCBL than in a NBL at both inboard and outboard locations. This is again consistent with the observations in Fig. 3. Moreover, the PDF curves for turbine 2 are, in general, flatter than the corresponding curves for turbine 1, reflecting higher standard deviation. Also, the PDF curves for turbine 2 are not as smooth, which is attributed to the enhanced turbulence experienced by the second turbine.

So far, we have discussed the statistics and PDF of local AOA at selected blade stations. These give an overall idea of how the blade loads and the integrated power are expected to reflect this behavior; however, one needs to look at the PSD of AOA to gain an insight into the frequency content in the time histories of the sectional AOAs. Figure 5 shows the PSD of computed AOAs for turbine 1 and spanwise locations r/R = 0.340 and r/R = 0.914 for both NBL and MCBL inflow. The sampling frequency was 50 Hz corresponding to the simulation time step of 0.02 s, thus resulting in 85,000 samples. In order to produce smooth spectra, 85 windows of 1,000 samples each were used, and the mean of the PSD of each of these windows was computed. Comparisons are again

performed for the two types of ALM spreading methods. Figure 6 shows the corresponding plots for turbine 2. For both turbines, both NBL and MCBL inflow conditions, and for each of the spreading methods, the dominant frequency inboard is the rotational frequency 1/rev, i.e. about 0.15 Hz (or 9 RPM). The higher harmonics of *n*(1/rev)* apart from the dominant frequency are also visible in Figs. 5-6 at the outboard station r/R = 0.91, while they are much less pronounced at the inboard station r/R = 0.34. This is attributed to the fact that the blade tip has a more sensitive response to smaller-scale ABL turbulence, which is in part due to the combination of a smaller blade chord outboard and higher velocities, both leading to a smaller time scale associated with the blade tip region. It can also be observed that the higher harmonics of turbine 2 are not perfectly aligned with the higher harmonics of rotational frequency. This is attributed to the variable rotor speed of turbine 2 in response to the turbulent wake from turbine 1. The frequency response and hence the PSD of integrated power is expected to comprise the various frequency responses at inboard as well as outboard locations. This will be further analyzed in section B2 on integrated quantities. For both turbines in Figs. 5 and 6, inboard as well as outboard, the NBL and MCBL stability states do not seem to result in a noticeable difference in the PSD; however, the spreading method affects the spectra predominantly at the outboard station r/R = 0.91 (Figs 5(c), 5(d), 6(c) and 6(d)). The PSD for the two spectra differ for frequencies higher than about 6 Hz. This means that the ALM method using ε/c^* is more sensitive to the higher frequencies (or smaller-scale turbulence) than the one using a constant Gaussian radius defined by $\varepsilon/\Delta_{grid}$. It is interesting to note that the ALM spreading methods do not affect

the PSD at the inboard station r/R = 0.340. This observation is in agreement with those made for the AOA variation along the blade span where tip loads (*r/R* > 0.85) are quite different between the two ALM methods. Therefore, a further investigation into the frequencies above 6 Hz is necessary to understand the turbulence scales and unsteady aerodynamics resolved by the two ALM approaches. To quantify the 'degree of unsteadiness', a convective time scale is defined [37] as the time taken to traverse half the local chord length by the local relative velocity, i.e.

$$t_c(r) = \frac{c(r)/2}{U_{rel}(r)} \quad . \tag{5}$$

The corresponding convective frequency is defined as:

$$f_c(r) = \frac{1}{t_c(r)} \tag{6}$$

Figures 5-6 show vertical lines at frequencies corresponding to different multiples of the local t_c. It is apparent that the ALM method using *ε/c** can sense frequencies corresponding to the time scales in the range of higher multiples of t_c at the outboard location. The peaks in this frequency range do not match the exact multiples of t_c. This can be attributed to the fact that the actual chord geometry is not meshed. It can only be established through a highly blade-resolved simulation whether these frequencies are manifestations of the accuracy of the ALM approaches used. It should be noted that the highest frequency sensed corresponding to the sampling frequency of 50 Hz might have missed further small-scale motions. A study with higher sampling frequency can potentially shed light on this; however, this would require smaller time steps, thus setting a more stringent requirement on the blade tip than traversing, at the

most, one grid cell per time step. Apart from the peaks of the frequencies discussed, it can be observed that the inertial sub-range of the spectra get prolonged for the ALM method using ε/c^*, meaning sensing smaller turbulence scales. The above observation holds true for both the turbines and both the ABL states.

B2. Integrated Quantities

The sectional blade loads, for the most part proportional to the sectional AOA, are integrated along the span yielding power, thrust, and root-flap bending moment, see Jha et al. **[**34**]**. Here, the time histories, statistics, and PSD of integrated power are discussed. The frequency response of the integrated power and its relation to the frequency response of sectional AOA is also addressed. Figure 7 shows the power histories of the two turbines for the two ABL states. In each subfigure, comparisons are made between the two ALM spreading methods. For both turbines, the power for the second turbine is lower than the first turbine due to a velocity deficit in the wake that has not fully recovered at turbine 2. This power drop for the downstream turbine (turbine 2) is more pronounced for the NBL than for the MCBL. This is attributed to the fact that, for the MCBL, higher turbulent mixing relative to the NBL helps in recovering the wake velocity deficit at a higher rate. Higher fluctuations in the power for both turbines are visible for MCBL flow, which is again associated with higher turbulence levels due to enhanced mixing as a result of surface heating. The effect of the ALM spreading method can also be observed. For each turbine and for each ABL state, constant Gaussian spreading according to the $\varepsilon/\Delta_{grid}$ criterion leads to slightly higher peaks, which is attributed to the over-prediction of blade tip loads as seen in Fig. 3. The

time trace of integrated power clearly shows a range of frequencies. The lower frequencies are attributed to the average large-eddy turnover time in the respective ABL flows, which are of higher amplitude in the MCBL flow compared to the NBL flow and attributed to higher vertical velocity fluctuations in the MCBL compared to the NBL. Similar to AOA, more insight about the frequencies can be gained from the spectra of integrated power. Figure 8 shows the PSD of the two turbines for the two ABL states and with comparisons between the two ALM spreading methods. Since the integrated power incorporates the accumulated effects of all three blades, the dominant frequency here is *3/rev*. It is apparent from Fig. 8 that the turbine rotation is responsible for the dominant PSD peak reflected at *3/rev* (or *0.45 Hz*). The higher harmonics of *n*(3/rev)* can also be seen and occur because of the fluctuating velocity components that result in a different incoming mean shear flow for every single blade revolution. These higher harmonics have most contributions from the outboard spanwise blade locations as observed in the spectra of AOAs in Figs. 5 and 6. Similar to the spectra of AOA, the peak frequencies for turbine 2 are not perfectly aligned with the harmonics of *3/rev*. The effect of the elliptic ALM spreading method according to a ε/c^* criterion can be observed for higher frequencies where the reduced tip loads compared to ALM spreading according to $\varepsilon/\Delta_{grid}$ in Fig. 3 are more sensitive to the turbulent eddies. The frequencies beyond 6-7 Hz resolved by the ALM method using ε/c^* are a combined effect of the sectional convective time scales and the response of the lower tip loads.

Figure 9 shows the mean, standard deviation, and the ratio of the two for the integrated power where the statistics comprise data from 300 s to 2,000 s of simulation

time. Comparisons are made for the two ABL states, i.e. NBL and MCBL, and the two spreading methods. The observations for the mean and standard deviations for the two turbines are in accordance with their respective time traces, i.e. the mean power for turbine 2 is smaller than that of turbine 1. This is more pronounced in NBL flow as the wake does not recover as quickly in the absence of enhanced vertical mixing due to surface heating. For turbine 1, the ABL stability state does not have as much effect as on turbine 2. The standard deviation in power for both the turbines is higher in MCBL flow compared to NBL flow. The absolute values of standard deviation for turbine 2 compared to turbine 1 may be misleading. It is therefore more instructive to look at standard deviation normalized by the corresponding mean power. For both ABL states, the ratio of standard deviation to mean power is almost twice as much for turbine 2 compared to turbine 1. With regards to the effect of the ALM spreading method, both the mean power and the standard deviation are affected for both turbines and both ABL states. In general, the elliptic spreading according to ε/c^* results in lower predicted values due to reduced tip loads. The numerical values are given in Tables 1 and 2, respectively. The difference in mean power due to the ALM spreading method is about 2.6 – 2.7 % for turbine 1 and about 3.90 - 4.26 % for turbine 2. A difference of about 4% is not insignificant for an array of wind turbines since it may result in an over-estimation of array efficiency. It is not surprising that turbine 2 exhibits an accumulated effect of differences in the ALM spreading methods as discrepancies in wake parameters downstream of turbine 1 are amplified through an additional ALM step at turbine 2.

It is hypothesized that the difference due to spreading would be further augmented if more turbines are placed downstream because of the accruing difference as mentioned above. Further simulations with more turbines may shed some light on this behavior but is beyond the scope of the current work that is meant to build the basis for uncertainty quantification in the wakes of wind turbines. Furthermore, previous work [16,17] has demonstrated the high sensitivity of integrated rotor power to the exact values for the const. in equation (4), which further adds to the uncertainty associated with the ALM. Note that, in this work, we are using best-practice values for both ALM spreading methods and focus on differences that are primarily associated with different tip loads.

Appendix A shows that the difference in high-frequency response of the two ALM spreading methods is not due to numerical discretization error. This is shown by analyzing the associated PSD of turbine power for a reference case with uniform inflow, i.e. no atmospheric turbulence.

B3. Wake Velocity Deficit

So far, we have looked exclusively at the loads and integrated quantities for the two turbines. We have discussed the differences in the sectional loads, integrated quantities, and the relation between them. It is equally important, however, to gain a deeper understanding of how the turbine wakes develop under different ABL stability states and what impact the ALM spreading methods have on the wake, and how the differences between them affect the performance of the downstream turbine. Figure 10 shows the mean axial velocity along vertical lines. The plots are shown at distances 2D

(a,c) and 6D (b,d) downstream of the respective turbines. Note that turbine 2 is located 7D downstream of turbine 1. It is interesting to note that Fig. 10(b) represents the flow conditions 1D upstream of turbine 2 (or 6D downstream of turbine 1). The small differences seen in the wake profiles between the two spreading methods, though, result in appreciable power differences in Tables 1 and 2. Comparisons are made again between the two ALM spreading methods for both NBL and MCBL flow conditions. The associated mean velocity profiles for the ABL precursor simulations (NBL and MCBL) are shown in Fig 1(b). It can be seen that the ALM spreading method has only a relatively small effect on the mean velocity profiles. Comparing the two ABL states, the wake recovery is higher for the MCBL than for the NBL; however, the velocity profiles in the near wake downstream of the two turbines are quite different. While 2D downstream of turbine 1 the effect of flow acceleration through the hub area is visible, it is minimized 2D downstream of turbine 2. This can be attributed to an enhanced turbulent mixing in the wake of turbine 1 before it interacts with turbine 2.

B4. Unsteadiness of Blade Loads

As outlined earlier, the turbulent inflow to the turbines is the primary cause of the unsteady blade loads, which are a contributor to blade fatigue. In this section, we study the influence of the ALM projection method and the ABL stability state on the unsteadiness of sectional blade loads. Since the transient flow leads to different velocity profiles at a given actuator point as the blades sweep through the atmospheric boundary layer, the resulting AOA and hence the blade loads are also transient at that actuator point. A natural choice to quantify the unsteadiness in the blade loads is,

therefore, the rate of change of AOA, i.e. $\dot{\alpha}(r)$. This can be converted to a non-dimensional reduced frequency which is defined as:

$$k(r) = 2\pi\left|\dot{\alpha}(r)\right| / \, f_c(r) = 2\pi\left|\dot{\alpha}(r)\right|\frac{c(r)/2}{U_{rel}(r)} \tag{7}$$

where c(r) is the local chord and U_{rel}(r) is the local resultant velocity.

Analogous to Fig. 4, Figure 11 shows the PDFs of the reduced frequency in wave space, *k*, for the two turbines and at the spanwise locations r/R = 0.340 and r/R = 0.914 representative of one inboard and one outboard station, respectively. Comparisons are performed for the two types of ALM projection method and the two ABL states. A vertical line is drawn at the cut-off reduced frequency of 0.05. The area under the curve above this cut-off, i.e. $k > 0.05$, is a measure of the relative duration of potentially unsteady effects. In order to quantify the unsteadiness, the percentage area under the PDF curve, above and below this $k = 0.05$ cut-off reduced frequency, was computed. Table 3 shows this for the two ABL states and the two ALM projection methods for the inboard as well as outboard location of turbine 1; Table 4 shows the same for turbine 2. For both turbines and both ABL states, the unsteadiness at the inboard location is less for the simulation with elliptic Gaussian spreading compared to the simulation with constant Gaussian spreading. This is opposite at the outboard location where the simulation with elliptic Gaussian spreading predicts considerably higher unsteadiness than that with constant spreading. This can be attributed to the fact that, when constant spreading is used in the ALM, the body force close to the blade tip is spread over a larger volume, and hence the small-scale fluctuations (higher frequencies)

associated with the tip loads are less responsive to the ABL turbulence as is the case for elliptic spreading. In general, for turbine 2, it can be observed that the unsteadiness is higher at the inboard location than at the outboard location for each ABL, both turbines and both projection methods. The unsteadiness for MCBL is, in general, higher except for the outboard location of turbine 2. It can also be observed that the unsteadiness at turbine 2 is substantially higher than at turbine 1, for both ABL states, blade locations, and projection methods. This is attributed to higher turbulence levels experienced by turbine 2 as discussed in Figs. 7- 9. Figure 12 shows the mean (a,b) and standard deviation (c,d) of reduced frequency at the two representative radial locations. These bar plots are consistent with the PDF curves in Fig. 11 and Tables 3 and 4. For example, a higher mean and standard deviation inboard corresponds to more unsteadiness and a wider PDF curve. The same observation holds true for turbine 2 compared to turbine 1.

It has to be kept in mind that that the computed reduced frequencies, *k*, are based on an 'instantaneous' blade responses, $\dot{\alpha}(r)$, thus neglecting a time lag in the respective blade loading. A natural question arises as to how the incorporation of a dynamic stall model such as that of Oye [37], also described in Hansen [38], might affect the analyses presented in this work and, particularly, differences in turbine power observed between the two ALM projection methods. Figure 13 shows representative dynamic responses of local lift coefficient, C_l, at r/R = 0.34 and r/R = 0.91 for turbine 1 for a sample α(t) in MCBL flow, computed with the ALM projection method based on ε/c*. It becomes evident that the C_l response behaves as quasi-steady, i.e. very little or no hysteresis in C_l response. The reason for this behavior is primarily attributed to the

fact that AOAs at these radial stations are well in the attached flow regime, see Fig. 3. It appears therefore that higher (reduced) frequencies are less important, see also PSD of AOA in Fig.6 showing the low energy content. Consequently, differences associated with the ALM projection method are unlikely to result in different dynamic response. Note, however, that this may be different for other wind turbine designs and operating conditions that exhibit high AOAs and true dynamic stall conditions.

IV. CONCLUSIONS

Actuator-line modeling (ALM) is becoming an increasingly important part of computational fluid mechanics tools that is expected to be accurate and computationally efficient in modeling and predicting the performance of multiple wind turbine arrays and entire wind farms. While a lot of effort has been given towards predicting wake velocity deficits and turbulence statistics downstream of wind turbines and deep into large wind farms, not much attention has been given to predicting the spanwise blade loads of individual turbine blades and their local response to variable atmospheric inflow conditions, and whether or not unsteady blade-section aerodynamics is of importance in conjunction with uncertainties in the ALM concept.

For two NREL 5-MW wind turbines separated by seven rotor diameters, it was found that a difference (or uncertainty) in mean turbine power of the order of 4 percent occurs as a result of the specific actuator line method. This difference was mainly attributed to a difference in local blade loads outboard of the r/R = 0.85 spanwise blade station.

As such, for the first turbine in an array, the uncertainty between particular actuator-line modeling approaches is of the same order as the variations associated with the atmospheric stability state itself. This is potentially important for estimating blade fatigue and associated O&M costs as well as array performance. This work also quantified, for the first time, the potential significance of unsteady aerodynamic effects through a reduced frequency defined by means of the rate-of-change of the sectional blade angle of attack. An improved actuator line method based on an equivalent elliptic chord distribution responds more sensitively to unsteady inflow conditions near the blade tip, which is important to monitor the structural health of the blades; however, actual differences in unsteady aerodynamics effects are small due to ranges in AOA and reduced frequency that makes the rotor blade tip section in particular behave quasi-steady. It should be noted that the authors used best-practice values for parameter settings in either ALM approach; more uncertainty is expected when deviating from these recommended settings. These differences, starting with the local blade angle of attack outboard of the r/R = 0.85 spanwise station, are propagated into the respective turbine wakes and are observed in the wake deficits. This gives confidence that the underlying OpenFOAM LES solver does not artificially (numerically) dissipate these differences.

The true message of this work to the wind energy community is the following: an uncertainty of only one percent in the performance of a large wind farm, for example the Horns Rev wind farm in Denmark, can cost an operator more than one million dollars per year. While the present work pushes the physical and accuracy limits of

state-of-the-art actuator-line modeling, there is a need for the wind energy community to quantify uncertainties for modeling accuracy of wind farm wake models that account for differences in ALM approaches and unsteady aerodynamics at blade sections. It is apparent that modeling accuracy is still not at a sufficient level, and the community of wind energy researchers is tasked with both finding innovations to the current modeling techniques that include unsteady aerodynamics but also to advance modeling fidelity on highly parallel computing systems and defining needs for experimental data campaigns to validate the various computational efforts.

V. APPENDIX

This appendix is intended to support the discussion concerning Figs. 5- 8, with respect to the small scales of the turbulent motion captured by the elliptic-planform based ALM approach. This was accomplished by performing simulations for each of the two ALM approaches with uniform inflow and with exactly the same grid and time step (and hence sampling frequency, *Fs*) as the simulations with ABL inflow.

Figure A1(a) shows the power histories for the two ALM approaches with uniform inflow. The y-axis has the same range as in Fig. 7. Small fluctuations around the mean are attributed to a small error associated with the interpolation of surrounding cell-centered physical quantities to the actuator points, an error common to all ALM approaches. Figure A1(b) shows a comparison of the spectra in response to uniform and ABL inflow for both ALM approaches. Turbine 1 and MCBL were chosen for comparison to uniform inflow. Since the sampling for uniform inflow was performed for 90 seconds

with a sampling frequency of 50 Hz, the total number of data points is 4,500. In order to get sharp spectra, an average of 90 windows of size, *ws*, 50 each were used. The spectra for uniform inflow do not follow the $5/3^{rd}$ law in the case of uniform inflow. This is well expected in the absence of any turbulence (see Fig A1 (a)). It is clear from Fig. A1(b) that high-frequency content seen in uniform-inflow simulations is indeed two orders of magnitude smaller than that due to atmospheric turbulence.

ACKNOWLEDGMENT

The authors are indebted to Dr. Matthew Churchfield from NREL for his invaluable help in performing the initial simulations and the many constructive comments on the manuscript.

The help and advice of Mr. Kirk Heller, system administrator in the Department of Aerospace Engineering at Penn State University, regarding the simulations on in-house high performance computing (HPC) clusters is greatly appreciated.

FUNDING

This work was supported by the U.S. Department of Energy (DOE) under program number DE-EE0005481 as part of the “Cyber Wind Facility” project at the Pennsylvania State University and in collaboration with the National Renewable Energy Laboratory (NREL).

NOMENCLATURE

ABL	Atmospheric boundary layer
ADM	Actuator disk method
ALM	Actuator line method
AR	Blade aspect ratio
AOA	Angle of attack, degrees
c	Blade chord, m
*c**	Equivalent elliptic-planform chord, m
CFD	Computational fluid dynamics
D	Rotor diameter, m
f_c	Blade sectional convective frequency, 1/s
k	Blade sectional reduced frequency, dimensionless
LES	Large-eddy simulation
MCBL	Moderately-convective boundary layer
NBL	Neutral boundary layer
NREL	National Renewable Energy Laboratory
PDF	Probability density function, dimensionless
PSD	Power spectral density, (physical quantity)^2/Hz
R	Blade radius, m
r	Local radius, m
RANS	Reynolds-Averaged Navier-Stokes

t_c	Blade sectional convective time scale, s
RPM	Revolutions per minute, 1/min
TKE	Turbulent kinetic energy, m^2/s^2
TSR	Tip speed ratio, $\Omega R/ V_{wind}$
U_{rel}	Blade sectional speed at actuator point, m/s
V_{wind}	Mean wind speed, m/s
V_{Hub}	Mean wind speed at hub height, m/s
ε	Gaussian spreading width, m
Δ_{grid}	Grid spacing, m
Δr	Actuator width, m
Ω	Rotational speed, rad/s

REFERENCES

[1] Rathmann, O., Frandsen, S. T., Barthelmie, R. J., 2007, "Wake Modelling for Intermediate and Large Wind Farms," Proceedings of the European Wind Energy Conference and Exhibition, Milan, Italy, May 7-10.

[2] Jensen, L. E., 2007, "Array Efficiency at Horns Rev and the Effect of Atmospheric Stability," Dong Energy, Fredericia, Denmark.

[3] Vijayakumar, G., Lavely, A., Jayaraman, B., Craven, B., Brasseur. J.G., 2014, "Blade Boundary Layer Response to Atmospheric Boundary Layer Turbulence on a NREL 5MW Wind Turbine Blade with Hybrid URANS-LES," AIAA 2014-0867.

[4] Lavely, A., Vijayakumar, G., Craven, B., Jayaraman, B., Jha, P. K., Nandi, T., Paterson, E.G., Brasseur, J.G., 2014, "Toward a Blade-Resolved Hybrid URANS-LES of the NREL 5-MW Wind Turbine Rotor within Large Eddy Simulation of the Atmospheric Boundary Layer," AIAA 2014-0869.

[5] Sørensen, J. N., and Shen, W. Z., 2002, "Numerical Modeling of Wind Turbine Wakes," ASME J. Fluids Eng., **124**, pp. 393-399.

[6] Shen, W. Z., Zhu, W. J., and Sørensen, J. N., 2012, "Actuator Line/Navier-Stokes Computations for the MEXICO Rotor: Comparison with Detailed Measurements," Wind Energy, **15** (5), pp. 811-825.

[7] Shen, W. Z., Mikkelsen, R., Sørensen, J. N., and Bak, C., 2005, "Tip Loss Corrections for Wind Turbine Computations," Wind Energy, **8**(4), pp. 457-475.

[8] Troldborg, N., Sørensen, J. N., and Mikkelsen, R., 2007, "Actuator Line Simulation of Wake of Wind Turbine Operating in Turbulent Inflow," J. Physics: Conf. Ser., **75**, p. 012063.

[9] Troldborg, N., Sørensen, J., and Mikkelsen, R., 2010, "Numerical Simulations of Wake Characteristics of a Wind Turbine in Uniform Flow," Wind Energy, **13** (1), pp. 86-99.

[10] OpenFOAM—The Open Source CFD Toolbox, Version 2.0.x, OpenCFD Ltd, a part of the ESI Group, 2013, http://www.openfoam.com.

[11] Churchfield, M. J., Lee, S., Michalakes, J., and Moriarty, Patrick J., 2012, "A Numerical Study of the Effects of Atmospheric and Wake Turbulence on Wind Turbine Dynamics," J. Turbulence, **13** (12), pp. 1-32.

[12] Churchfield, M. J., Moriarty, P. J., Vijayakumar, G., Brasseur, J., 2010, "Wind Energy-Related Atmospheric Boundary-Layer Large-Eddy Simulation Using OpenFOAM," National Renewable Energy Laboratory, Golden, CO, Report No. NREL/CP-500-48905.

[13] Churchfield, M. J., Lee, S., Moriarty, Patrick J., Martínez, Luis A., Leonardi, S., Vijayakumar, G. and Brasseur, J. G., 2012, "A Large-Eddy Simulation of Wind-Plant Aerodynamics," AIAA 2012-0537.

[14] Lee, S., Churchfield, Matthew J., Moriarty, Patrick J., Jonkman, J., and Michalakes, J., 2012, "Atmospheric and Wake Turbulence Impacts on Wind Turbine Fatigue Loadings," AIAA 2012-0540.

[15] Lee, S., Churchfield, Matthew J., Moriarty, Patrick J., Jonkman, J., and Michalakes, J., 2013, "A Numerical Study of Atmospheric and Wake Turbulence Impacts on Wind Turbine Fatigue Loadings," ASME J. Sol. Energy Eng., **35** (13), 031001.

[16] Martínez, Luis A., Leonardi, S., Churchfield, Matthew J., and Moriarty, Patrick J., 2012, "A Comparison of Actuator Disk and Actuator Line Wind Turbine Models and Best Practices for Their Use," AIAA 2012-0900.

[17] Martínez, Luis A., Churchfield, Matthew J., and Leonardi, S., 2014, "Large eddy simulations of the flow past wind turbines: actuator line and disk modeling," Wind Energy, Published online in Wiley Online Library (wileyonlinelibrary.com). DOI: 10.1002/we.1747.

[18] Segalini, A., and Alfredsson, P.H., 2013, "A simplified vortex model of propeller and wind-turbine wakes," J. Fluid Mech., **725**, pp. 91-116. doi:10.1017/jfm.2013.182.

[19] Okulov, V.L., and Sørensen, J.N., 2010, "Maximum efficiency of wind turbine rotors using Joukowsky and Betz approaches," J. Fluid Mech., **649**, pp. 497–508. doi:10.1017/S0022112010000509.

[20] Lu, H., and Porté-Agel, F., 2011, "Large-Eddy Simulation of a Very Large Wind Farm in a Stable Atmospheric Boundary Layer," Phys. Fluids, **23**, p. 065101.

[21] Meyers. J., and Meneveau, C., 2010, "Large Eddy Simulations of large wind-turbine arrays in the atmospheric boundary layer," AIAA-2010-827.

[22] Calaf, M., Meneveau, C., and Meyers. J., 2010, "Large eddy simulation study of fully developed wind-turbine array boundary Layers," Phys. Fluids, **22**, 015110. doi: 10.1063/1.3291077.

[23] Meyers. J., and Meneveau, C., 2012, "Optimal turbine spacing in fully developed wind farm boundary layers," Wind Energy, **15**, pp. 305–317. DOI: 10.1002/we.469.

[24] VerHulst, C. and Meneveau, C., 2014, "Large eddy simulation study of the kinetic energy entrainment by energetic turbulent flow structures in large wind farms," Phys. Fluids, **26**, 025113. doi: 10.1063/1.4865755.

[25] Nathan, J., Bautista, M., Masson, C., and Dufresne, L., 2014, "Study of the near wake of a wind turbine in ABL flow using the actuator line method," J. Physics: Conf. Ser., **524**, 012141. doi:10.1088/1742-6596/524/1/012141.

[26] Okulov, V.L, and Sørensen,J.N, 2007, "Stability of helical tip vortices in a rotor far wake," J. Fluid Mech., **576**, pp. 1–25. doi:10.1017/S0022112006004228.

[27] Viola, F., Iungo, G. V., Camarri, S., Porté-Agel, F., and Gallaire, F., 2014, "Prediction of the hub vortex instability in a wind turbine wake: stability analysis with eddy-viscosity models calibrated on wind tunnel data," J. Fluid Mech., **750**, R1, doi:10.1017/jfm.2014.263.

[28] Hong, J., Toloui, M., Chamorro, L.P., Guala, M., Howard, K., Riley, S.,Tucker, J., and Sotiropoulos, F., 2014, "Natural snowfall reveals large-scale flow structures in the wake of a 2.5-MW wind turbine," NATURE COMMUNICATIONS, **5**, 4216. DOI: 10.1038/ncomms5216.

[29] Chatelain, P., Backaert, S., Winckelmans, G., and Kern, S., 2013, "Large Eddy Simulation of Wind Turbine Wakes," Flow Turbulence Combust, **91** (3), pp. 587–605. DOI 10.1007/s10494-013-9474-8.

[30] Stevens, R.J.A.M., Graham, J., and Meneveau, C., 2014, "A concurrent precursor inflow method for Large Eddy Simulations and applications to finite length wind farms," Renewable Energy, **68**, pp. 46-50. doi: 10.1016/j.renene.2014.01.024.

[31] Leishman, J.G., 2002, "Challenges in modelling the unsteady aerodynamics of wind turbines," Wind Energy, **5**, pp. 85–132. doi: 10.1002/we.62.

[32] Jha, P. K., Churchfield, M. J., Moriarty, P. J., and Schmitz, S., 2013, "Accuracy of State-of-the-Art Actuator-Line Modeling for Wind Turbine Wakes," AIAA-2013-0608.

[33] Jha, P. K., Churchfield, M. J., Moriarty, P. J., and Schmitz, S., 2014, "Guidelines for Actuator Line Modeling of Wind Turbines on Large-Eddy Simulation-type Grids," ASME J. Sol. Energy Eng., **136** (3), 031003.

[34] Jha, P. K., Churchfield, M. J., Moriarty, P. J., and Schmitz, S., 2014, "The Effect of Various Actuator-Line Modeling Approaches on Turbine-Turbine Interactions and Wake-Turbulence Statistics in Atmospheric Boundary-Layer Flow," AIAA 2014-0710.

[35] Jha, P. K., Duque, E. P. N., Basioum, J. L., and Schmitz, S., 2015, "Unraveling the Mysteries of Turbulence Transport in a Wind Farm," Energies, **8** (7), pp. 6468-6496.

[36] Jonkman, J., Butterfield, S., Musial, W., and Scott, G., 2009, "Definition of a 5-MW Reference Wind Turbine for Offshore System Development," National Renewable Energy Laboratory, NREL Report No. TP-500-38060.

[37] Leishman, J.G., 2006, *Principles of Helicopter Aerodynamics*, Cambridge Aerospace Series, 2nd edition, p.427.

[38] Oye, S., 1991, "Dynamic stall, simulated as a time lag of separation," in K.F. McAnulty (ed) *Proceedings of the 4th IEA Symposium on the Aerodynamics of Wind Turbines*, ETSU-N-118, Harwell Laboratory, Harwell, UK.

[39] Hansen, M.O.L., 2008, Aerodynamics of Wind Turbines, Earthscan Publishing, 2nd edition, p. 96.

Figure Captions List

Fig. 1 OpenFOAM-LES computational setup and precursor data used for turbine-turbine interaction problem

Fig. 2 Instantaneous flow field in a horizontal plane at hub height (t = 2,000 sec, NBL inflow).
The quantity shown is the component of vorticity normal to the plane.

Fig. 3 Mean and standard deviation (error bar) of blade angle of attack (AOA)

Fig. 4 Probability density function (PDF) of blade angle of attack (AOA)

Fig. 5 Power spectral density (PSD) of angle of attack (AOA) at selected spanwise stations

Fig. 6 Power spectral density (PSD) of angle of attack (AOA) at selected spanwise stations

Fig. 7 Power histories for turbine-turbine interaction problem

Fig. 8 Power spectral density (PSD) of turbine power

Fig. 9 Mean and standard deviation of turbine power

Fig. 10 Mean streamwise velocity distributions in the vertical direction

Fig. 11 Probability density function (PDF) of reduced frequency

Fig. 12 Mean and standard deviation of reduced frequency

Fig. 13 Example of C_l response to Dynamic Stall Model of Oye.

Fig. A1 Power response of NREL 5-MW turbine subject to uniform inflow

Table Caption List

Table 1 Mean power for the turbines

Table 2 Standard deviation in power for the turbines

Table 3 Percentage area under PDF curve, above and below the cut-off reduced frequency of k = 0.05, Turbine 1

Table 4 Percentage area under PDF curve, above and below the cut-off reduced frequency of k = 0.05, Turbine 2

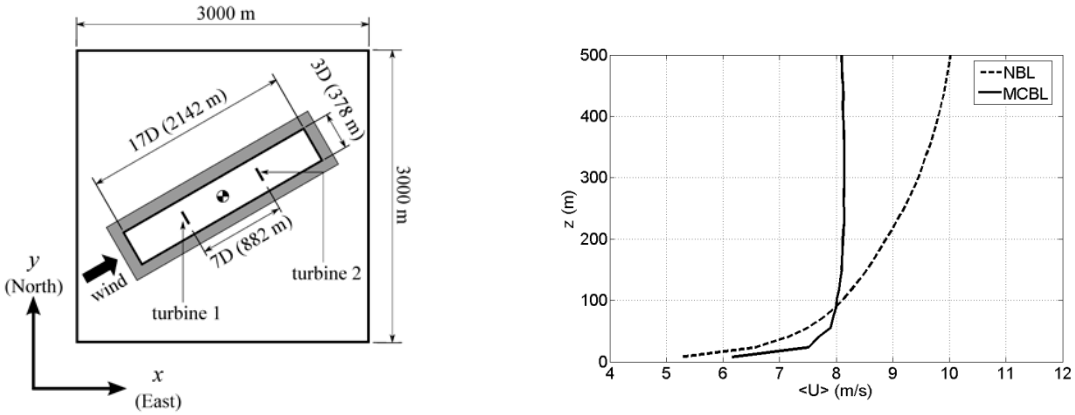

(a) Computational domain

(b) Mean velocity profiles (U_{hub} = 8 m/s)

Figure 1. OpenFOAM-LES computational setup and precursor data used for turbine-turbine interaction problem

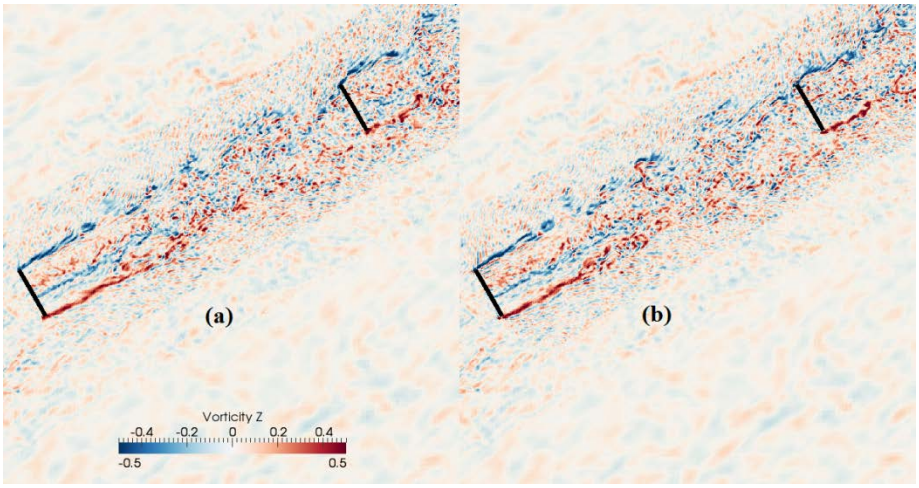

(a) $\varepsilon/\Delta_{grid}$ = const. **(b) ε/c^*= const.**

Figure 2. Instantaneous flow field in a horizontal plane at hub height (t = 2,000 sec, NBL inflow). The quantity shown is the component of vorticity normal to the plane.

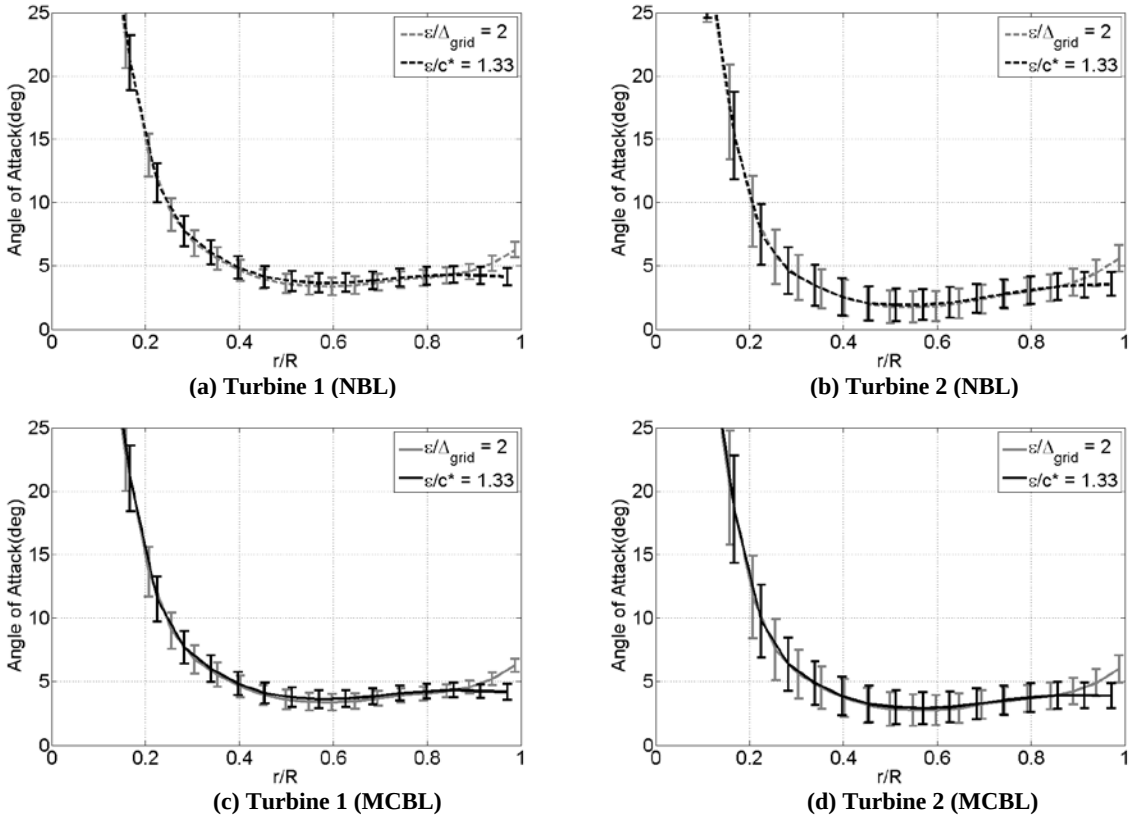

(a) Turbine 1 (NBL) **(b) Turbine 2 (NBL)**

(c) Turbine 1 (MCBL) **(d) Turbine 2 (MCBL)**

Figure 3. Mean and standard deviation (error bar) of blade angle of attack (AOA)

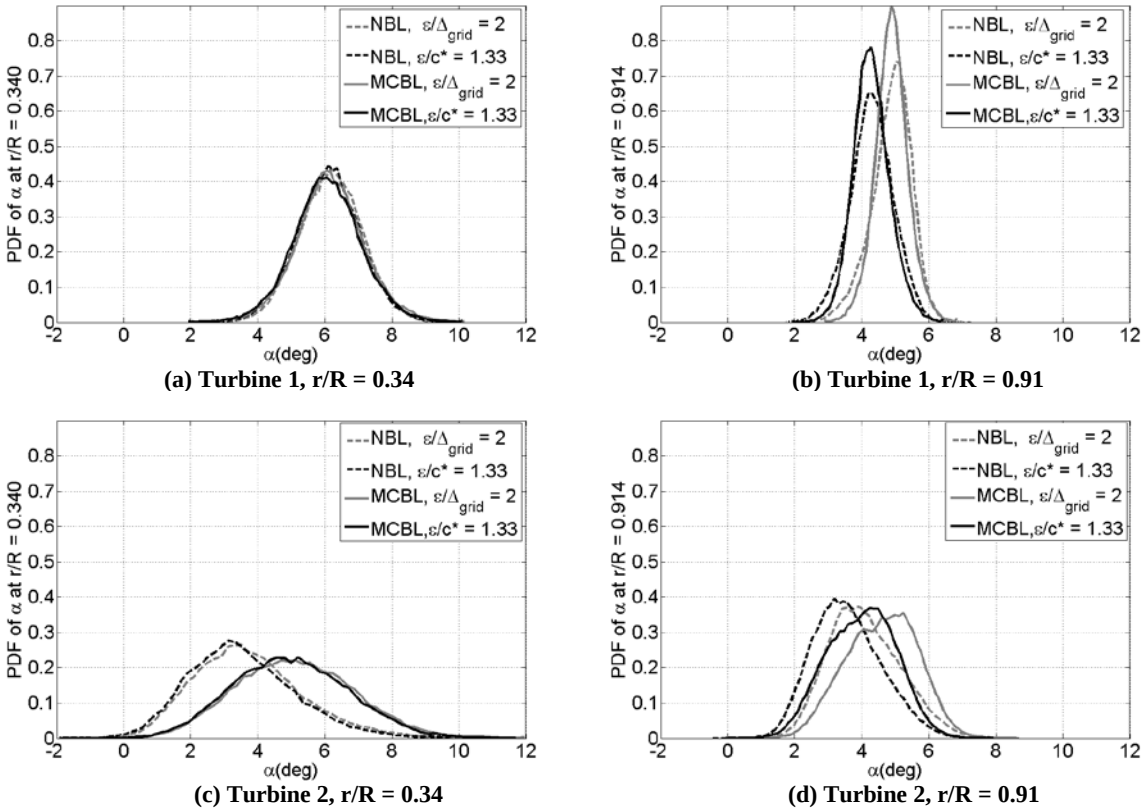

(a) Turbine 1, r/R = 0.34 **(b) Turbine 1, r/R = 0.91**

(c) Turbine 2, r/R = 0.34 **(d) Turbine 2, r/R = 0.91**

Figure 4. Probability density function (PDF) of blade angle of attack (AOA)

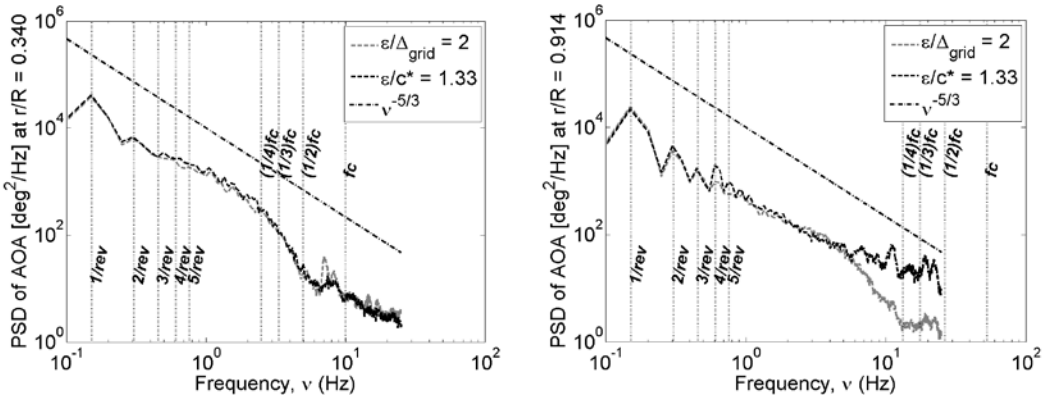

(a) Turbine 1, r/R = 0.34 (NBL) **(b) Turbine 1, r/R = 0.91 (NBL)**

(c) Turbine 1, r/R = 0.34 (MCBL) **(d) Turbine 1, r/R = 0.91 (MCBL)**

Figure 5. Power spectral density (PSD) of angle of attack (AOA) at selected spanwise stations

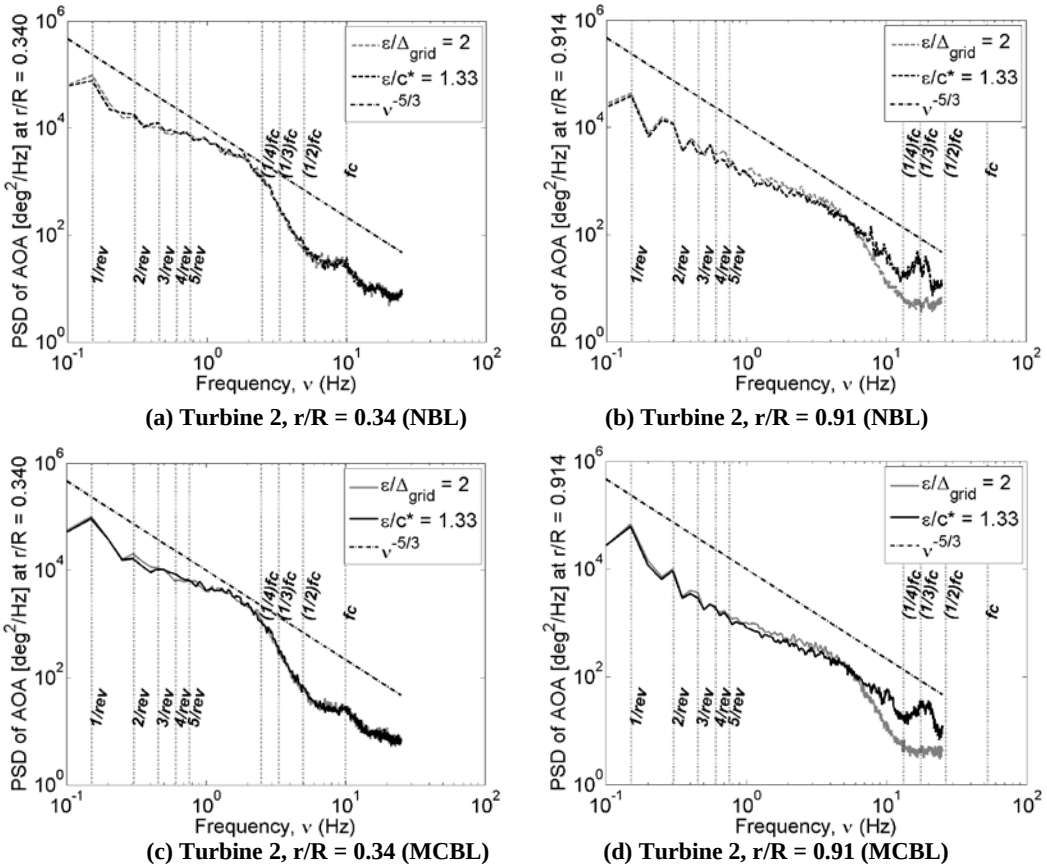

(a) Turbine 2, r/R = 0.34 (NBL) **(b) Turbine 2, r/R = 0.91 (NBL)**

(c) Turbine 2, r/R = 0.34 (MCBL) **(d) Turbine 2, r/R = 0.91 (MCBL)**

Figure 6. Power spectral density (PSD) of angle of attack (AOA) at selected spanwise stations

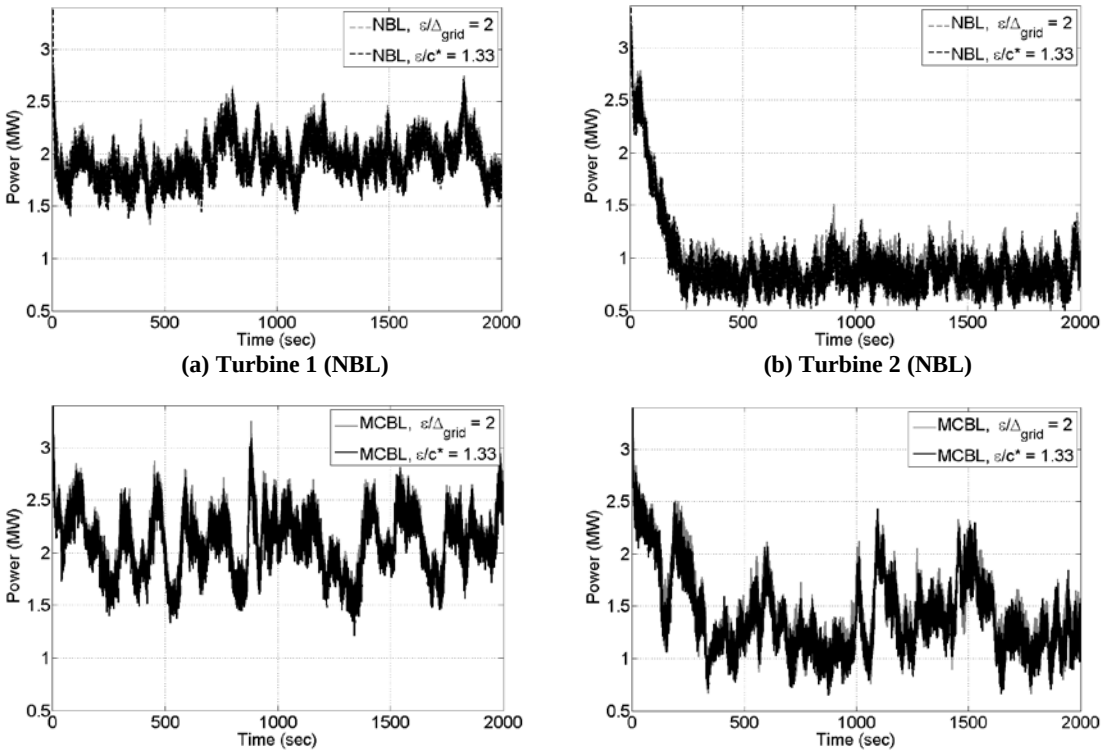

(a) Turbine 1 (NBL) **(b) Turbine 2 (NBL)**

(c) Turbine 1 (MCBL) **(d) Turbine 2 (MCBL)**

Figure 7. Power histories for turbine-turbine interaction problem

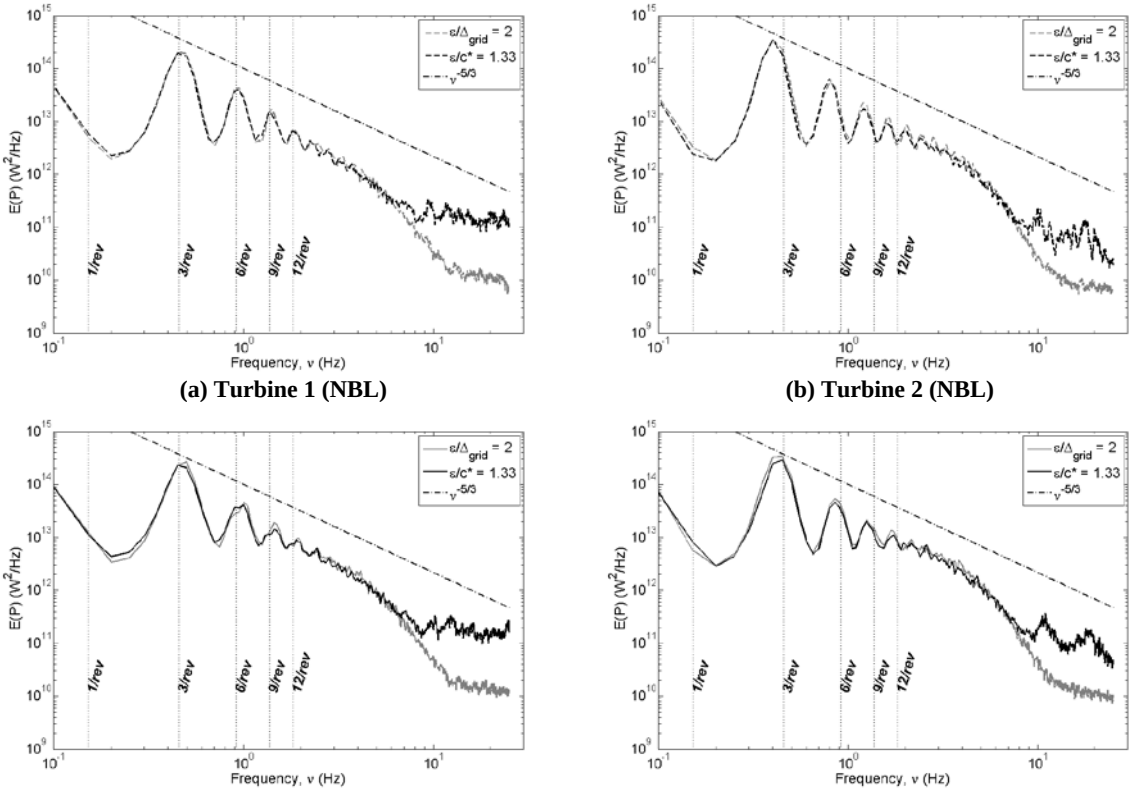

(a) Turbine 1 (NBL) **(b) Turbine 2 (NBL)**

(c) Turbine 1 (MCBL) **(d) Turbine 2 (MCBL)**

Figure 8. Power spectral density (PSD) of turbine power

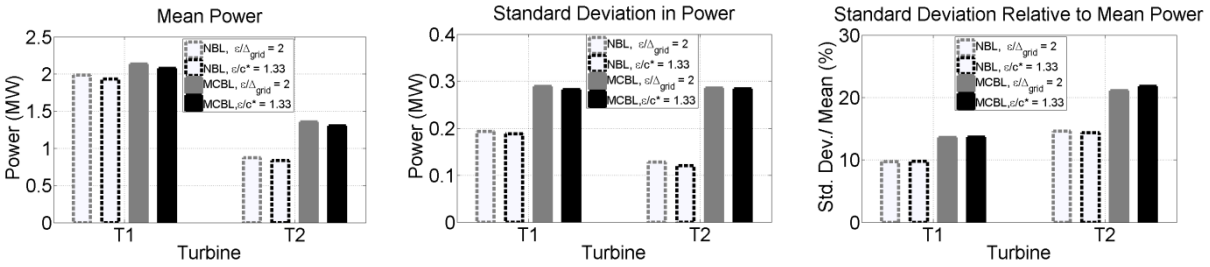

(a) Mean turbine power **(b) Std. dev. in turbine power** **(c) Std. dev. relative to mean power**

Figure 9. Mean and standard deviation of turbine power

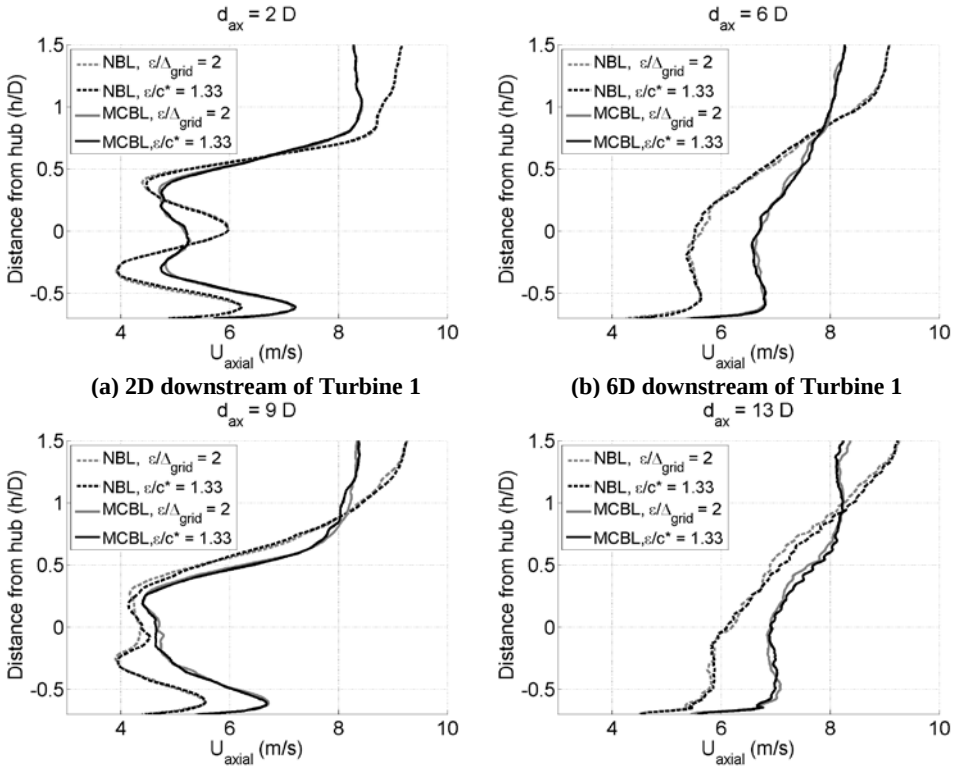

(a) 2D downstream of Turbine 1 **(b) 6D downstream of Turbine 1**

(c) 2D downstream of Turbine 2 **(d) 6D downstream of Turbine 2**

Figure 10. Mean streamwise velocity distributions in the vertical direction

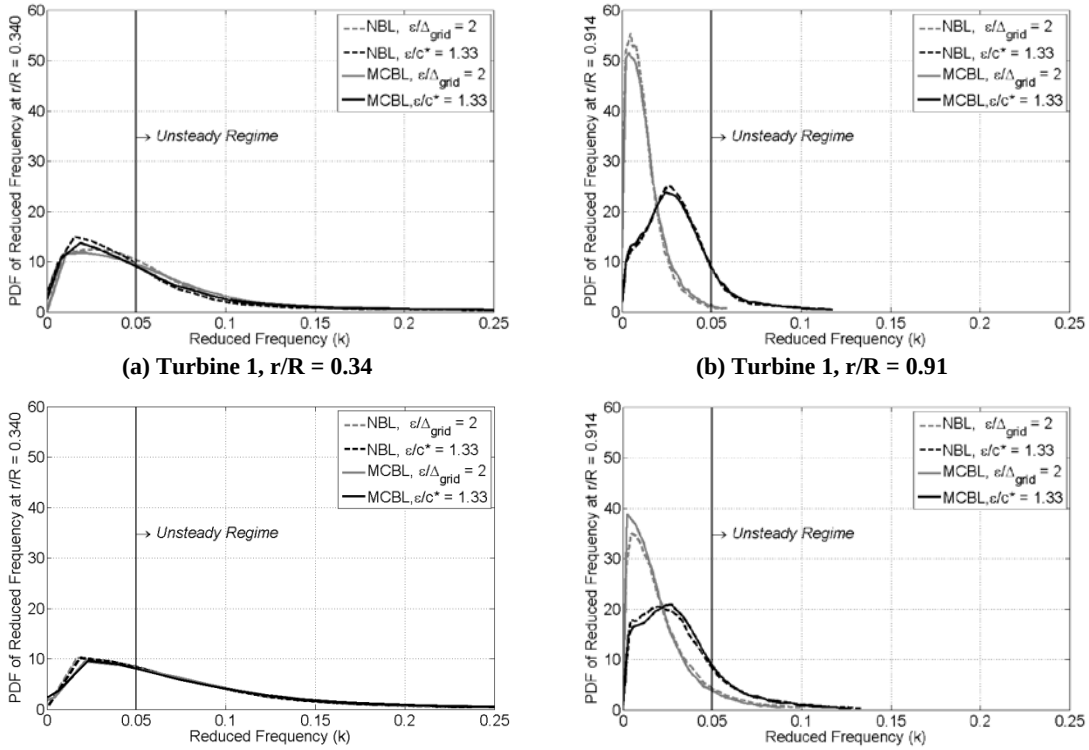

(a) Turbine 1, r/R = 0.34 **(b) Turbine 1, r/R = 0.91**

(c) Turbine 2, r/R = 0.34 **(d) Turbine 2, r/R = 0.91**

Figure 11. Probability density function (PDF) of reduced frequency

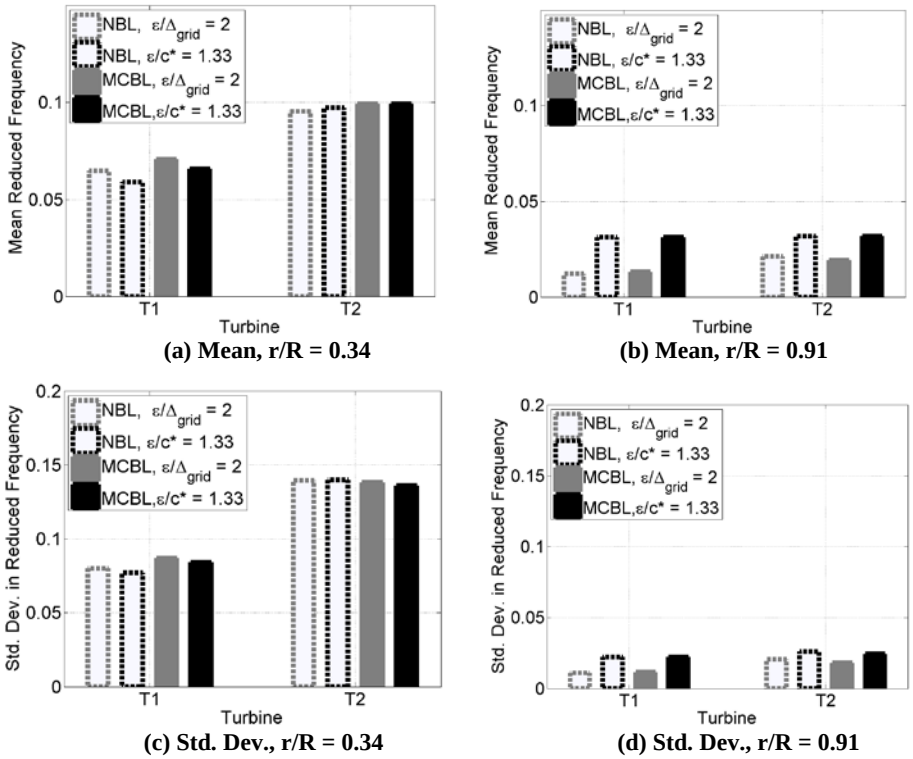

(a) Mean, r/R = 0.34 **(b) Mean, r/R = 0.91**

(c) Std. Dev., r/R = 0.34 **(d) Std. Dev., r/R = 0.91**

Figure 12. Mean and standard deviation of reduced frequency

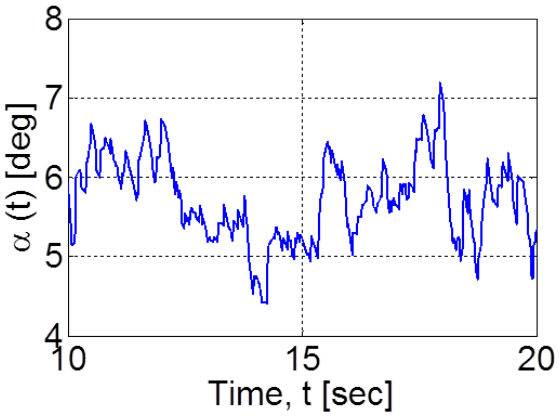

(a) Sample AOA(t) for Turbine 1, r/R = 0.34 (MCBL)

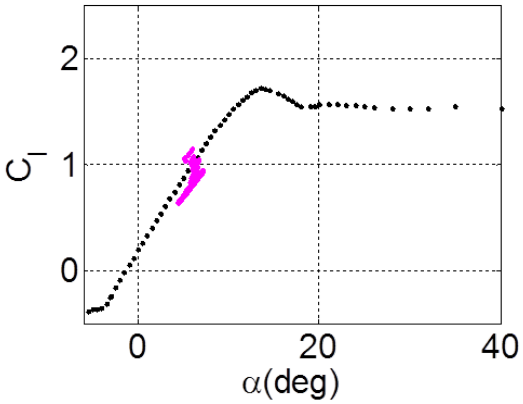

(b) Dynamic C_l for Turbine 1, r/R = 0.34 (MCBL)

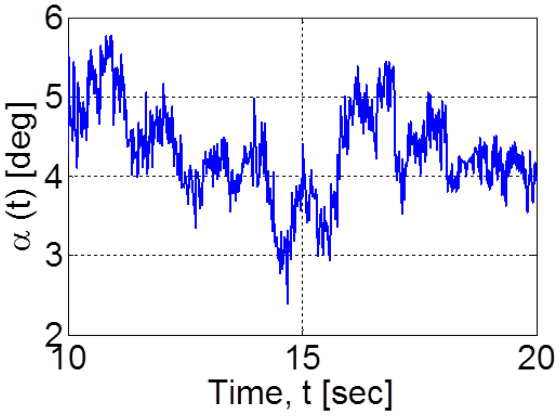

(c) Sample AOA(t) for Turbine 1, r/R = 0.91 (MCBL)

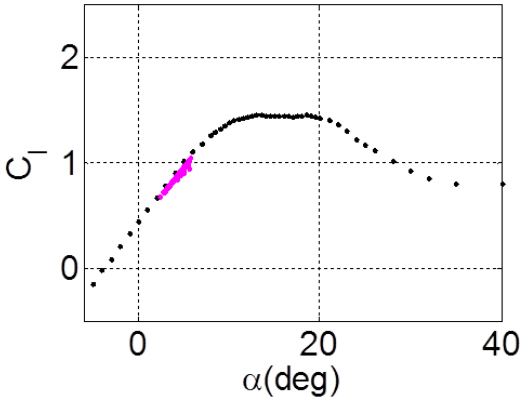

(d) Dynamic C_l for Turbine 1, r/R = 0.91 (MCBL)

Figure 13. Example of C_l response to Dynamic Stall Model of Oye.

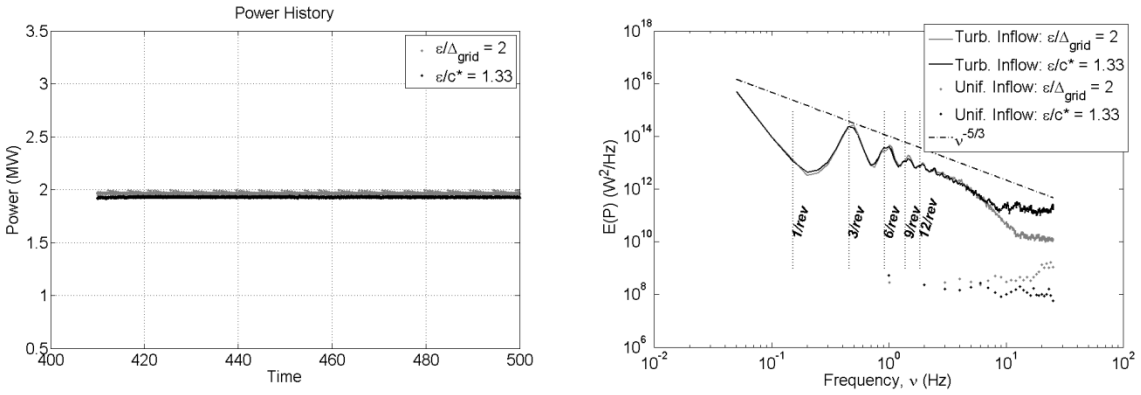

(a) Power History **(b) Power spectral density (PSD)**

Figure A1. Power response of NREL 5-MW turbine subject to uniform inflow.

Table 1: Mean power for the turbines

Mean Power (MW)		**Turbine 1**	**Turbine 2**
NBL	Constant ε	1.9820	0.8731
	Elliptic ε	1.9305	0.8359
	% Difference	***2.60***	***4.26***
MCBL	Constant ε	2.1294	1.3554
	Elliptic ε	2.0719	1.3025
	% Difference	***2.70***	***3.90***

Table 2: Standard deviation in power for the turbines

Std. Dev. in Power (MW)		**Turbine 1**	**Turbine 2**
NBL	Constant ε	0.1926	0.1273
	Elliptic ε	0.1878	0.1196
	% Difference	***2.49***	***6.05***
MCBL	Constant ε	0.2883	0.2853
	Elliptic ε	0.2821	0.2669
	% Difference	***2.15***	***6.45***

Table 3: Percentage area under PDF curve, above and below the cut-off reduced frequency of k = 0.05, Turbine 1

Turbine 1		Inboard (r/R = 0.34)		Outboard (r/R = 0.91)	
		$k \leq 0.05$	k > 0.05	$k \leq 0.05$	$k > 0.05$
NBL	Constant ε	63.69	36.31	99.67	0.33
	Elliptic ε	64.52	35.48	88.02	11.98
MCBL	Constant ε	54.20	45.80	99.41	0.59
	Elliptic ε	64.12	35.88	87.17	12.83

Table 4: Percentage area under PDF curve, above and below the cut-off reduced frequency of $k = 0.05$, Turbine 2

Turbine 2		Inboard (r/R = 0.34)		Outboard (r/R = 0.91)	
		$k \leq 0.05$	$k > 0.05$	$k \leq 0.05$	$k > 0.05$
NBL	Constant ε	42.23	57.77	92.08	7.92
	Elliptic ε	43.37	56.63	84.09	15.91
MCBL	Constant ε	42.90	57.10	94.55	5.45
	Elliptic ε	44.29	55.71	83.75	16.25